Optics and Lasers in Engineering 151 (2022) 106889

Contents lists available at ScienceDirect

Optics and Lasers in Engineering

journal homepage: www.elsevier.com/locate/optlaseng

Hyperspectral imaging via a multiplexing digital micromirror device

Wen Chen [a], Ming-Jie Sun [a,*], Wei-Jie Deng [b,c], Hai-Xiang Hu [b,c], Li-Jing Li [a], Xue-Jun Zhang [b,c]

[a] Department of Opto-electronic Engineering, Beihang University, Beijing 100191, China
[b] Changchun Institute of Optics, Fine Mechanics and Physics, Chinese Academy of Sciences, Changchun 130033, China
[c] Key Laboratory of Optical System Advanced Manufacturing Technology, Chinese Academy of Sciences, Changchun 130033, China

ARTICLE INFO

Keywords:
Computational ghost imaging
Spectral imaging
Digital mircomirror device

ABSTRACT

Spectral imaging technique, which retrieves both spatial and spectral information of a scene or an object, is an important tool in applications such as food inspection, vegetation monitoring and geographic remote sensing. Most spectral imaging systems have a complex system architecture, in which different components are used for different functions, limiting the efficiency of information retrieval. Here, we propose a hyperspectral imaging system with a simple architecture, where a multiplexing digital micromirror device functions both as a spatial light modulator for spatial imaging and a diffractive grating for spectral measuring simultaneously. The proof-of-principle system contains a group of lenses, a digital micromirror device and a one-dimensional detector array, and is capable of performing 128 × 128 pixel resolution hyperspectral imaging over the visible spectrum with an experimental 3.73 nm spectral resolution. Furthermore, by using a compressive sampling strategy, continuous real-time spectral video is performed with a frame-rate up to 10 Hz. The concise architecture of the proposed system, with the potential to be easily extended to both ultraviolet and infrared, offers an alternative scheme to manufacture low-cost, compact, hyperspectral imagers.

1. Introduction

Both spatial and spectral information provides us crucial knowledges of the world. Chromatic digital cameras obtain both information simultaneously by placing an absorbing color-filter array (a.k.a. the Bayer filter) on top of a detector array [1], because photo-electronic sensors are only light intensity sensitive. However, only three bands, usually red, green and blue wavelengths, are measured by chromatic digital cameras. Spectral imaging, which obtain images with much more spectral information in every pixel of a scene than chromatic digital cameras do, is an important technique to survey scenes and probe object properties [2,3]. Specifically, multispectral imaging obtains images at spaced narrow bands, whereas hyperspectral imaging surveys a scene using contiguous bands which cover a continuous range of wavelength, producing a spectral distribution for each pixel in the scene. We noted that there are various definitions for hyperspectral, usually it refers to obtaining contiguous spectral information along a wide range of wavelength with a spectral resolution 10 nm, however, some only consider systems with spectral resolution smaller than 1 nm as hyperspectral. In this work, hyperspectral is referred as its usual definition.

There are two types of spectral imagers, scanning and non-scanning. The scanning type can be further divided into two sub-types, which are spatial scanning and spectral scanning. The spatial scanning spectral imagers [4–6] use push-broom scanners, i.e., line-scan systems, or whisk-broom scanners, i.e., point-scan systems to obtain spectral information using a prism or a grating in each measurement and then form (x, y, λ) three-dimensional (3D) spectral image cube with sequential measurements over time. The spectral scanning ones [7–9] capture one image at a certain spectral band in each measurement and then acquire different bands temporally by using a liquid-crystal tunable filter or an acousto-optical one. The scanning spectral imagers are not suitable for dynamic applications because the spectral image cube is acquired over time, and they usually have complicated system structures.

The non-scanning spectral imagers, i.e., snapshot spectral imaging [10–13] use a detector array to capture a perspective projection of the (x, y, λ) data in a single snapshot, from which the 3D spectral image cube can be reconstructed. The major advantage of non-scanning spectral imagers is that the one-shot acquisition enables its dynamic applications. However, the manufacturing cost of the devices as well as the computational cost to reconstruct the spectral image cube are high.

Ghost imaging [14–16] reconstructs an image by measuring the correlations between the scene and a series of two-dimensional (2D) masks. Though outperformed by digital cameras in conventional photography, the flexibilities demonstrated by ghost imaging making it particularly well-suited for non-conventional applications, such as multi-wavelength

* Corresponding author.
E-mail address: mingjie.sun@buaa.edu.cn (M.-J. Sun).

https://doi.org/10.1016/j.optlaseng.2021.106889
Received 9 May 2021; Received in revised form 8 November 2021; Accepted 21 November 2021
Available online 29 November 2021

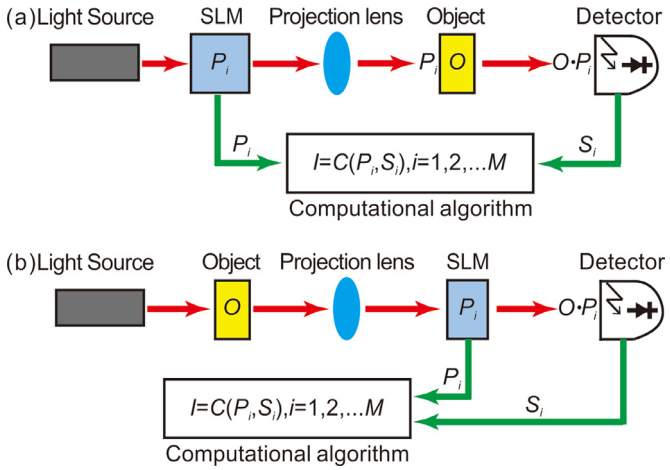

Fig. 1. Schematic of computational ghost imaging. (a) The light source is modulated by a spatial light modulator (SLM) with different masks. And the structured illumination is projected on the object by a projection lens. The reflected or transmitted light of the object is measured by a single-pixel detector. A computational algorithm uses the knowledge of the masks along with their corresponding measurements to reconstruct an image of the object. (b) The object is first illuminated by the light source, then imaged by a camera lens onto the focal plane, where a SLM is placed. The SLM modulates the image by displaying different masks, and the reflected or transmitted light of the modulated image are collected and measured by a single-pixel detector. The image of the object can be reconstructed with the knowledge of the masks and the corresponding measurements.

imaging [17], 3D profiling [18–20] and adaptive imaging [21]. Recently, there are some interesting developments in spectral imaging techniques utilizing computational ghost imaging scheme [22]. Due to the single-pixel detection nature [23,24] of the scheme, it is easy for a ghost imaging system to perform spectral dispersion without disturbing the spatial information. Ghost imaging based spectral imaging works include spectral scanning via a rotating color wheel [25], dispersion using a grating [26], two spatial light modulators for spectral ghost imaging [27], using ground glass as a random grating [28], and multispectral measurement with a spectrometer [29]. Nevertheless, fundamentally these works utilized ghost imaging as a conventional camera, and acquired the spatial-spectral 3D image cube with an extra optical component, which jeopardized measuring efficiency as and increased the system complexity.

In this work, we propose a hyperspectral computational ghost imaging system, in which a digital-micromirror-device (DMD) multifunctions as a spatial light modulator for spatial imaging and a 2D grating for spectrum measuring spontaneously. The architecture of the hyperspectral imaging system is simplified with the multiplexing DMD, its capability of dynamic imaging is demonstrated and further enhanced by performing sparse sampling in computational ghost imaging.

2. Theory

2.1. Principle of computational ghost imaging

In computational ghost imaging, it is the resolution of the masks on a spatial light modulator that determines the spatial resolution of the reconstructed image. These masks are either projected on a scene by a projector lens as structured illumination [22,29] as shown in Fig. 1(a), or displayed at the focal plane of a camera lens as modulations [30,31] as shown in Fig. 1(b). The reconstruction of an image can be performed by algorithms of various sophistications [29,32,33] among which the simplest is to weight each mask P_i by its related measurement S_i of a "bucket" detector, which records the total light intensity of the superposition between the scene and the mask. The image I is then reconstructed by summing these weighted P_i as

$$I = \sum_{i=1}^{M} S_i \cdot P_i, \tag{1}$$

where M is the number of measurements the ghost imaging system recorded sequentially in time. The masks used can be either partially correlated [15,16,22,29] or orthogonal [17,23,33,34]. Practically, a DMD is usually used in ghost imaging works [17–21,24–26] because its display rate is much larger than that of a liquid-crystal based spatial light modulator, especially when the masks to be displayed are binary [31,33].

2.2. Spectral dispersion via a DMD

Beside displaying fast switching masks, a DMD is sometimes used as a diffractive component, which is due to its micromirror arrangement [35–38]. It can be modeled as a double-ruled diffractive grating [35]. The first is a 2D grating of Cartesian geometry, where each micromirror is a diffraction spot with a pitch p between adjacent micromirrors [39], and the second is a blazed grating caused by the +12°/-12° flipping of the micromirrors along their hinges [40].

However, in order to simply the spectral information retrieval in this work, we limit its grating effect to one-dimensional (1D) by disabling partial of the micromirrors, illustrated as grey mirrors in Fig. 2(a). Specifically, the micromirrors arrayed in one row along x direction is a 1D grating with its grating constant $d = \sqrt{2}p$, and the y distance between the adjacent two gratings is set to be $3\sqrt{2}p$ so that the optical path difference is longer than the coherent length of the LED [41], and only incoherent intensity superposition happens among the diffraction patterns yielded by the paralleled 1D gratings. A chromatic diffraction pattern can be observed at the Fraunhofer plane of the DMD by illuminating a collimated beam from a white LED onto the DMD, and Fig. 2(b) shows the 0th and ±1st order of the diffraction pattern recorded at the Fraunhofer plane of the DMD. Experimental results demonstrate that the normalized intensity distributions of ±1st order (solid red and green in Fig. 2(c)) versus wavelength are in a good agreement with the ground truth spectrum (dash black in Fig. 2(c)), which is the product of the white LED spectrum, the transmissive property of the relay lenses and the spectral responsivity of the recording CCD. The spectral broadening is caused by the non-strictly collimated white light and the finite numbers of micromirrors on the DMD.

One important feature of the DMD revealed in this work is that even when displaying different masks, the DMD exhibits same diffractive characteristics, i.e., similar intensity distributions along the spectrum at 1st order diffraction. In this work, 32,768 Hadamard masks are generated by setting the '-1' elements to '0' in a 16384 × 16384 Hadamard matrix [42], and then reformatting each row of the matrix into a 128 × 128 2D mask. Each mask is followed by its inverse (where the elements of '1' and '0' are reversed), therefore 32,768 masks in total. 32,768 spectral intensity distributions are obtained when these Hadamard masks are displayed on DMD. By comparing these distributions to the +1st order diffraction intensity distribution in Fig. 2(c), we found that most of these distributions are not dramatically deviated from the +1st order diffraction, as shown in Fig. 2(d), with their average RMSE being 1.7%. This feature enables the DMD to being multiplexed in our proposed spectral imaging system both as a spatial light modulator for computational ghost imaging and a grating for spectrum measuring.

The spectral resolution of the grating illustrated in Fig. 2(a) is determined by the specifications of the DMD and how well the white light is collimated. The half angular size of ±1st order diffraction is $\Delta\theta_{\text{diff}}=\lambda/(N d\cos\theta)$, where λ is the wavelength, N is the average number of features in a 1D grating, d is the grating constant, and $\theta_{\text{diff}}=\arcsin(\lambda/d)$ is the deviation angle of ±1st order diffraction. The angular dispersion is $\mathrm{d}\theta/\mathrm{d}\lambda=1/d\cos\theta_{\text{diff}}$. Therefore, the distinguishable angular size of a given wavelength at ±1st order diffraction is

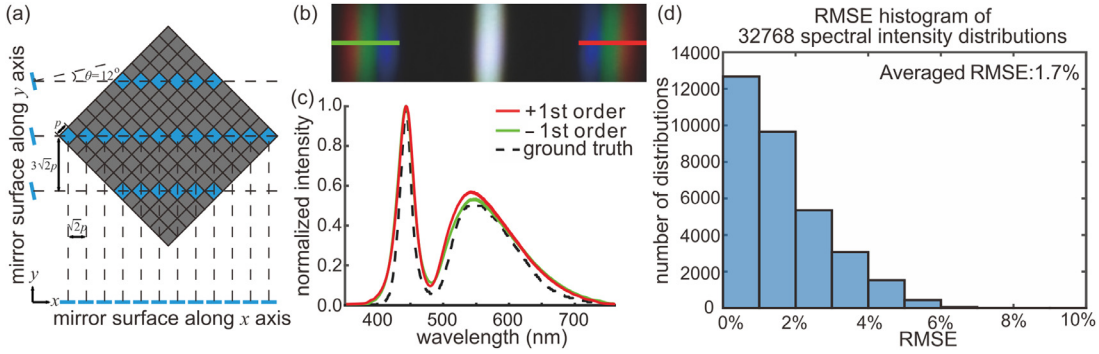

Fig. 2. Spectral dispersion of a white LED source with a digital micromirror device (DMD). (a) The grating model of a DMD used in this work. Blue squares are enabled micromirrors, grey squares are disabled ones, p is the DMD mirror pitch. (b) A photograph of the 0th, ±1st orders diffraction of a white LED source. (c) Normalized intensities of ±1st order diffraction pattern versus wavelength, compared to the ground truth. (d) The RMSE histogram of 32,768 spectral intensity distributions, which are obtained when the DMD displayed 32,768 different Hadamard masks, with respect to the +1st order diffraction intensity distribution in (c) (For interpretation of the references to color in this figure legend, the reader is referred to the web version of this article).

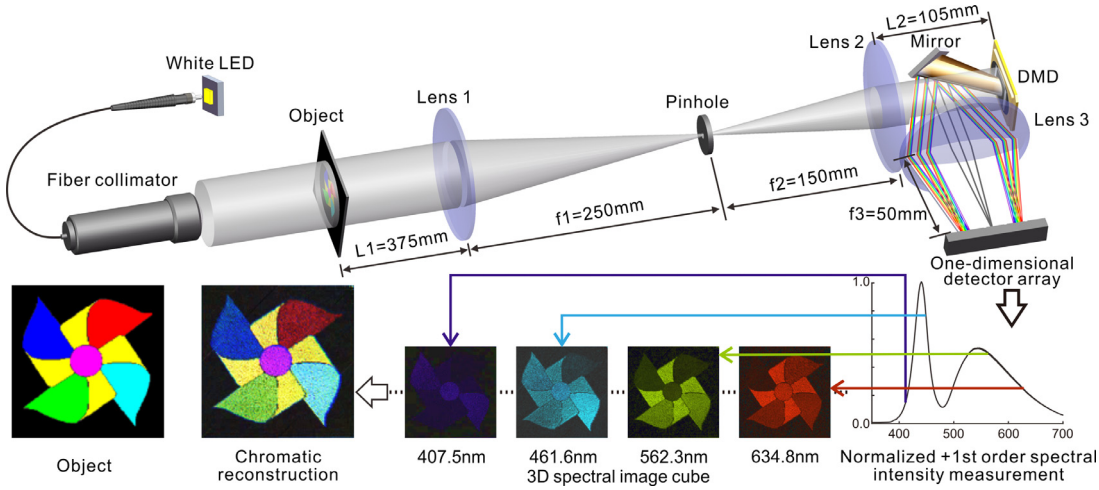

Fig. 3. Experimental setup of the proposed hyperspectral imaging system. A white LED source (OSRAM CSLMN1.TG, 10 W) is collimated by a fiber collimator (WYOPTICS 84UV, fiber diameter 50 μm, f_c = 100 mm), and illuminates a chromatic object. The DMD is located in the conjugate position of the object (DLPC410, micromirror array 1024 × 768, pitch 13.7 μm, operating at 20 KHz) by Lens 1 with f_1 = 250 mm and Lens 2 with f_2 = 150 mm. The DMD provides mask modulation for imaging and diffraction for spectral measuring. The diffraction pattern of the modulated light is formed at the focal plane of Lens 3 with f_3 = 50 mm, and its intensity distribution of 0th and ±1st order is recorded by a 1D detector array (Basler raL2048-48gm, pixel resolution 2048 × 1, pitch 7 μm, sampling at 40 KHz). Combining the knowledges of the modulation masks and the corresponding spectral intensity distributions, a series of images at different wavelengths can be reconstructed to form a 3D spectral image cube, which in turn can be fused into one chromatic image.

$\Delta\theta=\Delta\theta_{\text{diff}}+\Delta\theta_{\text{light}}$, where $\Delta\theta_{\text{light}}$ is the angular divergence of the collimated light, and the spectral resolution of the system proposed here is

$$\varepsilon = \left(\Delta\theta_{\text{light}} + \Delta\theta_{\text{diff}}\right) d\cos\theta_{\text{diff}}, \tag{2}$$

3. Result

3.1. System setup and spectral resolution

The experimental setup of the hyperspectral imaging system we proposed is illustrated in Fig. 3. The light emitted from a white LED (OSRAM CSLMN1.TG, 10W) is directly coupled into a fiber collimator (WYOPTICS 84UV, fiber diameter 50 μm, f_c=100 mm), and the collimated beam illuminates a chromatic transmissive object. The illuminated object is then imaged by Lens 1 and Lens 2 (f_1=250 mm, f_2=150 mm) onto the surface of a DMD (DLPC410, micromirror array 1024 × 768, pitch 13.7 μm, operating at 20 KHz). The pinhole between Lens 1 and 2 is to keep background noise out of the system. The image is modulated by a series of masks displayed on the DMD, and here 32,768 Hadamard masks with a 128 × 128 pixel resolution are generated and used here for differential measurement [31,34] in order to reduce fluctuations in ambient light levels. The modulated images are reflected by a mirror and their diffraction distributions are formed on the focal plane of Lens 3 (f_3=50 mm). A 1D detector array (Basler raL2048-48gm, pixel resolution 2048 × 1, pitch 7 μm, sampling at 40 KHz) is placed at the focal plane to record the 0th and ±1st order spectral intensity distribution of each modulation. Combining the knowledges of the Hadamard masks and their corresponding spectral intensity distributions, images at different wavelengths are reconstructed using Eq. (1) to form the 3D spectral image cube. A chromatic image can be further formed by fusing these images according to their wavelengths, as shown in Fig. 3.

The spectral resolution of the experimental system is calculated by the specifications and verified using the experimental measurements. The angular divergence of the collimated light is calculated to be 50 μm/100 mm = 0.5mrad, with its FWHM being 0.25mard. By replacing the object with an interference filter (central wavelength 422 nm, FWHM 4 nm), a light spot is recorded at the pinhole by a CMoS (Daheng MER-1220-32U3M, pixel resolution 4024 × 3036, pixel pitch 1.85 μm),

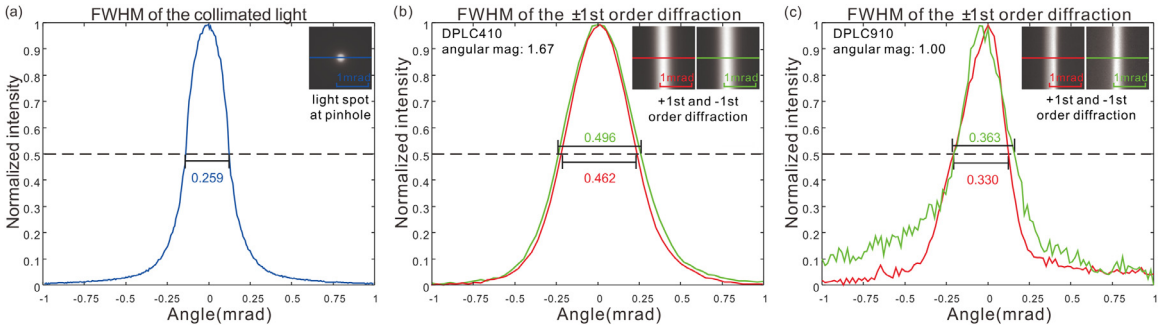

Fig. 4. Experimental spectral resolution analysis of the proposed hyperspectral imaging system. (a) The FWHM of the collimated white light is measured to be 0.26mrad. (b) With DPLC410 and 1.67 angular magnification, the FWHM of the ±1st order diffraction at 422 nm are measured to be 0.462mrad and 0.496mrad. Their average is 0.479mrad, led to a 9.26 nm spectral resolution. (c) With a DLP910 DMD and 1.0 angular magnification, the FWHM of the ±1st order diffraction at 422 nm are measured to be 0.33mrad and 0.363mrad. Their average is 0.347mrad, led to a 3.73 nm spectral resolution. The measurements are in a good agreement with the theoretical calculations.

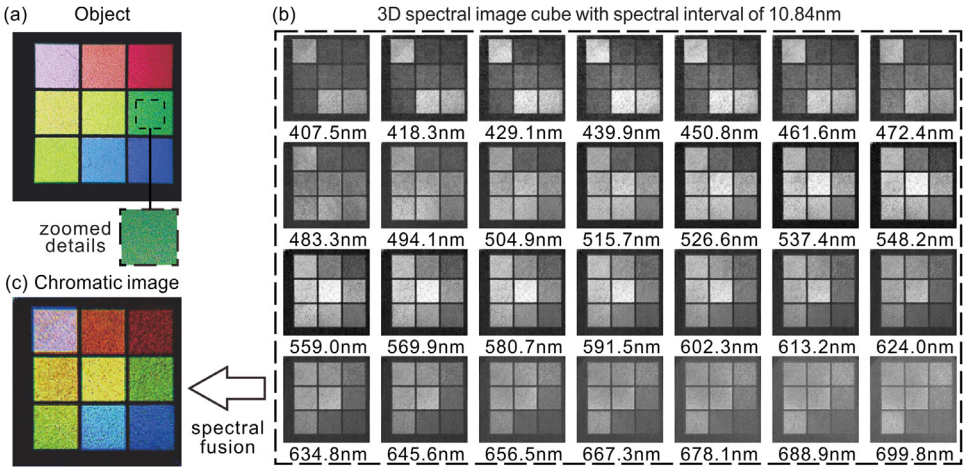

Fig. 5. Hyperspectral images reconstructed by the proposed hyperspectral imaging system. (a) A photo of the object, taken by a single lens reflex digital camera. Zoomed details showed that the printed surface of the object is grainy. (b) 3D spectral image cube reconstructed by the proposed hyperspectral imaging system. The center wavelength of each image is given. The spectral interval between two consecutive images is 10.84 nm, corresponding to 4 pixels on the 1D detector array. (c) A chromatic image of the object is fused from the 3D spectral image cube by transferring the center wavelength YMCK values and then weighted summing these values of all spectral images to yield the fused chromatic image.

as shown in Fig. 4(a). The FWHM of the measured angular divergence of the collimated light is determined as $\Delta\theta_{\text{light}} = 0.259$mrad by dividing the spot size with f_1, which is a good agreement with the calculation. For the experimental system illustrated in Fig. 3, the grating constant $d = \sqrt{2}p$=19.34 μm, the average number of features in one grating $N = 384$, leading to a half angular size of ±1st order diffractions $\Delta\theta_{\text{diff}} = 0.057$mrad. The angular divergence of the collimated light at the focal plane of Lens 3 is $0.25 \times 1.67 = 0.418$mrad, where 1.67 referred to the angular magnification determined by f_1/f_2. The distinguishable angular size at ±1st order diffraction is $\Delta\theta = \Delta\theta_{\text{diff}} + \Delta\theta_{\text{light}} = 0.475$mrad. By placing the CMoS at the focal plane of Lens 3, the diffraction pattern is recorded, as shown in Fig. 4(b). The FWHM of ±1st order diffractions are 0.462 and 0.496 mrad, and their average is 0.479mrad, which are in a good agreement with the calculation. Consequently, the experimental spectral resolution of the proposed system is determined by Eq. (2) as 9.26 nm.

To reach the full spectral resolution potential of the proposed system, Lens 2 is replaced with another lens of 250 mm focal length, leading to a 1.0 angular magnification. DLPC410 is replaced with another model DLPC910 (DLPC410, micromirror array 2560 × 1600, pitch 7.6 μm, operating at 10 KHz). In this case, the grating constant $d = 10.75$ μm, the average number of features in one grating $N = 800$, leading to a half angular size of ±1st order diffractions $\Delta\theta_{\text{diff}}$=0.049mrad. The angular divergence of the collimated light at the focal plane of Lens 3 is 0.25mrad and the distinguishable angular size at ±1st order diffraction is $\Delta\theta = 0.299$mrad. The experimental diffraction pattern is recorded, as shown in Fig. 4(c), with the FWHM of ±1st order diffractions are 0.33 and 0.363mrad, and their average is 0.347mrad. Considering the noise exhibited in this measurement, the experimental angular size is deemed to be coincident with the calculation. The experimental spectral resolution is improved to 3.73 nm.

It is worth mentioning that the spectral resolution of the proposed system, though wavelength related, is majorly limited by the divergence of the collimated light. It has been demonstrated that the spectral resolution can be enhanced by performing deconvolution on the measured spectral intensity distributions [43,44].

3.2. Experimental results

In the following experiments, the system setup illustrated in Fig. 3 is used. Specifically, the angular magnification of Lens 1 and Lens 2 combination is 1.67 to ensure the signal-to-noise for image reconstruction, DPLC410 is used for the real-time performance of the system. The spectral resolution of the system is 9.26 nm, as analyzed and measured in the previous section.

In one experiment, the object is a plastic film printed with color blocks, as shown in Fig. 5(a). 32,768 masks, containing a complete Hadamard set and its inverse, are used for spatial modulation. Combining the ±1st order spectral intensity distribution recorded by the 1D detector array and the knowledge of the Hadamard masks, the 3D spectral image cube within the spectral range between 400 and 700 nm, as shown in Fig. 5(b), is reconstructed using Eq. (1). The DMD displays modulation masks at 20 kHz rate, and the total time for data acquisition and transfer is ~1.8 s. Due to the linear superposition nature of Eq. (1), the image reconstruction is performed parallelly to the data acquisition and transfer in order to improve the imaging speed of the proposed system. Furthermore, taking advantage of the multicore CPU

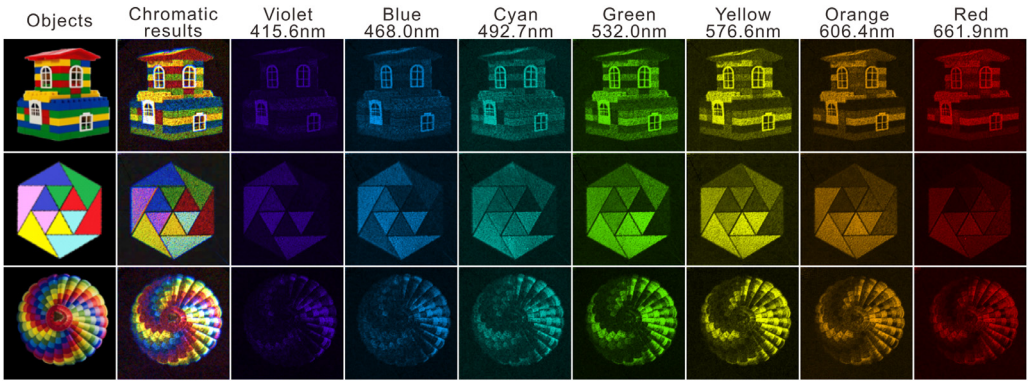

Fig. 6. Rainbow bands spectral images reconstructed by the proposed hyperspectral imaging system. The spectral widths are different for the rainbow bands, and for the proposed system, different numbers of pixels need to be summed accordingly to reconstruct the spectral images(For interpretation of the references to color in this figure, the reader is referred to the web version of this article).

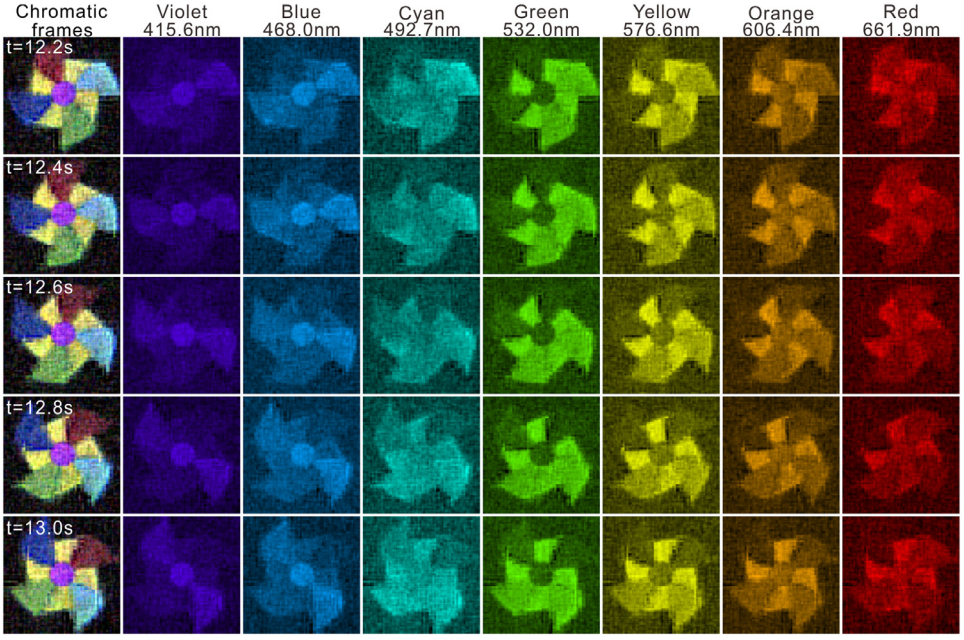

Fig. 7. Dynamic spectral imaging at 5Hz frame rate of an object rotating at 90°/s.

calculating power, the reconstruction for the 3D spectral image cube can be performed parallelly within itself, that is, the image reconstructions of different spectrum are independent to each other and can be carried out parallelly using the multicore CPU. Here, using a multicore CPU (Intel i5-7400, base frequency 3.0 GHz, 4 cores, 4 threads) and MATLAB platform, the reconstruction of 28 spectral images illustrated in Fig. 5(b) is performed within ~1.4 s, shorter than acquisition and transfer time, meaning that the image reconstruction doesn't slow down the image speed of the proposed system.

The images are of 128 × 128 pixel resolution, determined by the pixel resolution of the Hadamard mask. The pixel pitch of the 1D detector array is 7 μm, corresponding to 2.71 nm spectral resolution for the system described in Fig. 3. However, the spectral resolution determined by the optical system is measured to be 9.26 nm, therefore the measured intensities of 4 pixels are added to yield one spectral image, and the spectral interval between two consecutive reconstructed images is 10.84 nm. The spectral image cube can be further fused into a chromatic image of the object, as shown in Fig. 5(c). There are many sophisticated methods to perform image alignment and fusion in spectral imaging [45–48]. Here, the chromatic visualization is performed by transferring the center wavelength of every spectral image to a combination of YMCK values and then weighted summing these spectral images to yield the fused chromatic image. Interestingly, it fitted how the object is manufactured originally, that is the object is printed with a color laser printer, which operated under YMCK mode. It is worth mentioning that the noise exhibited in Fig. 5(c) is partially due to the noise during the experimental measurements, partially due to the grainy surface formed by the toner of the laser printer. Zoomed details of the object, recorded by a single lens reflex digital camera, verified that the printed surface of the object is grainy indeed, as shown in Fig. 5(a).

One problem hyperspectral imaging facing is the huge amount of data needed to be recorded, processed, and stored. In Fig. 5, dozens of spectral images are reconstructed individually before a chromatic image can be formed. Sometimes, the image processing speed is the priority of the system while only several spectral bands are needed. In such cases, the proposed system can simply sum the measured intensities of pixels, which corresponded to the spectral bands needed to be obtained, and reconstruct the required spectral images using Eq. (1). Rather than reconstructing and fusing a huge number of consecutive spectral images, Fig. 6 demonstrated that the proposed system obtained the spectral images of discrete rainbow bands by performing only seven reconstructions.

It is worth mentioning that the spectral widths are different for the rainbow bands, that is violet 380–450 nm, blue 450–485 nm, cyan 485–

500 nm, green 500–565 nm, yellow 565–590 nm, orange 590–625 nm, red 625–700 nm [49]. For the proposed system, the rainbow spectral widths corresponded to 26, 13, 6, 24, 9, 13, and 28 pixels of the 1D detector array. For each band, the measured intensities of the corresponding pixels are summed to used as Si in Eq. (1), regardless the spectral width, to reconstruct the spectral image.

Another challenge for most conventional spectral imaging systems is to meet the demands of real-time applications. The major obstacle is that the 2D detector array, which retrieves (x, y, λ) 3D data in a scanning manner, has a low readout rate [50]. The proposed hyperspectral imaging system also retrieves (x, y, λ) 3D data in a scanning manner due to its single-pixel detection imaging scheme. However, the 1D detector array used in the proposed system, which has a 40 kHz readout rate, is no longer the limiting factor. The 20 kHz modulation rate of the multiplexing DMD became the bottle neck.

More interestingly, computational ghost imaging scheme is capable of compressive sampling [30,51], which reconstructs images with sparse measurements and therefore further improves real-time performance of the proposed system. In this experiment, by applying the evolutionary compressive sensing in our previous work [18], which chooses a subset of the Hadamard masks having the most significances in the previous frame along with a fraction of randomly selected ones, real-time spectral imaging with a dynamic object (an object rotating at 90˚/s) is performed. A continues real-time spectral video with 5 Hz frame-rate is obtained using 4096 masks, equivalent to a 12% compression ratio (first half of Supplementary Movie 1). Fig. 7 showed a sample of consecutive spectral images in rainbow bands and their chromatic fusions from the spectral video. Importantly, however, spectral imaging can be performed using fewer masks to achieve higher frame-rates if required, for instance using 2048 masks provides 10 Hz video (second half of Supplementary Movie 1).

4. Conclusion and discussion

In this work, the specifications of the DMD hinder further improvements of the system performance. It is experimentally demonstrated here the spectral resolution can be improved by replacing the DLPC410 0.7XGA DMD chip with the DLPC910 0.9WQXGA chip. The inherent trade-off between spatial resolution and the frame-rate is limited by the modulation rate of the DMD. These two specifications can be enhanced by using other fast-switching devices. Attempts of addressing this problem with other fast-switching devices, such as LED array [24] and optical phase array [52], have been explored.

It is worth mentioning that during the experiments, we use non-strictly collimated white LED beam to illuminate the objects, which are chromatic films printed with a color laser printer with YMCK toners. These facts also limited the resulting images in visible spectrum with degraded spectral and spatial resolutions. With collimated sunlight and natural objects, we are expecting to obtain spectral images with a better quality from ultraviolet to infrared wavelength because the spectral range of DLP chips covers all wavelengths from 350 to 2500 nm. However, one needs to make sure that the illuminating spectral range is within (λ,2λ) so that ±1st order pattern does not overlap with its ±2nd. In other words, the shortest spectrum is (350 nm, 700 nm) and the longest is (1250 nm, 2500 nm).

In this work, the DMD is used as a one-dimensional grating to avoid partial coherent effect of the white LED source. The DMD will be used similarly if the proposed system is to work under sunlight. For limiting the grating effect to one-dimensional, a special spatial coding method is proposed, as shown in Fig. 2(a). Therefore, only 1/6 micro-mirrors are used, a relatively poor sensitivity is the main disadvantage of this system. However, if a supercontinuum laser source is used, the DMD can be used as a two-dimensional grating, and the system energy efficiency will be further improved by the 12˚ blazing angle.

In this work, we have proposed a hyperspectral imaging system via a multiplexing DMD, which provides mask modulation and spectral diffraction simultaneously. The experimental results demonstrate the feasibility of the proposed system to perform hyperspectral imaging for dynamic applications. With a concise architecture containing a group of lenses, a DMD and a linear detector array, the proposed system scheme can potentially be applied to manufacture compact, cost-effective, high performance spectral imaging devices.

Declaration of Competing Interest

The authors declare that they have no known competing financial interests or personal relationships that could have appeared to influence the work reported in this paper.

CRediT authorship contribution statement

Wen Chen: Software, Validation, Investigation, Data curation, Writing – original draft. **Ming-Jie Sun:** Conceptualization, Methodology, Validation, Data curation, Writing – review & editing, Visualization, Supervision, Project administration, Funding acquisition. **Wei-Jie Deng:** Formal analysis, Writing – review & editing, Visualization. **Hai-Xiang Hu:** Software, Writing – review & editing, Resources. **Li-Jing Li:** Resources, Writing – review & editing, Supervision. **Xue-Jun Zhang:** Resources, Writing – review & editing, Project administration.

Acknowledgments

M.-J. Sun acknowledges the support from National Natural Science Foundation of China (Grant No. 61922011) and Open Research Projects of Zhejiang Lab (Grant No. 2021MC0AB03).

Supplementary materials

Supplementary material associated with this article can be found, in the online version, at doi:10.1016/j.optlaseng.2021.106889.

References

[1] B.E. Bayer. Color imaging array. U.S. Patent No. 3971065 (1976).
[2] Wolfe WL. Introduction to imaging spectrometers. Opt Photonics News 1997;9(10):47. doi:10.1117/3.263530.
[3] Brady DJ. Optical imaging and spectroscopy. Wiley-Interscience; 2009. doi:101002/9780470443736.
[4] Mouroulis P, Green RO, Chrien TG. Design of push broom imaging spectrometers for optimum recovery of spectroscopic and spatial information. Appl Opt 2000;39(13):2210–20. doi:10.1364/AO.39.002210.
[5] Shaw GA, Burke HK. Spectral imaging for remote sensing. Linc Lab J 2003;14(1):3–28.
[6] Fowler JE. Compressive pushbroom and whiskbroom sensing for hyperspectral remote-sensing imaging. In: Proceedings of the IEEE international conference on image processing (ICIP); 2014. p. 684–8. doi:10.1109/ICIP.2014.7025137.
[7] Gebhart SC, Thompson RC, Jansen AM. Liquid-crystal tunable filter spectral imaging for brain tumor demarcation. Appl Opt 2007;46(10):1896–910. doi:10.1364/AO.46.001896.
[8] Sigernes F, Ivanov Y, Chernouss S, Trondsen T, Roldugin A, Fedorenko Y, Kozelov B, Kirillov A, Kornilov I, Safargaleev V, Holmen S, Dyrland M, Lorentzen D, Baddeley L. Hyperspectral all-sky imaging of auroras. Opt Express 2012;20(25):27650–60. doi:10.1364/OE.20.027650.
[9] Dekemper E, Loodts N, Opstal BV, Maes J, Vanhellemont F, Mateshvili N, Franssens G, Pieroux D, Bingen C, Robert C, Vos LD, Aballea L, Fussen D. Tunable acousto-optic spectral imager for atmospheric composition measurements in the visible spectral domain. Appl Opt 2012;201251(25):6259–67. doi:10.1364/AO.51.006259.
[10] Gao L, Kester RT, Hagen N, Tkaczyk TS. Snapshot image mapping spectrometer (IMS) with high sampling density for hyperspectral microscopy. Opt Express 2010;18(14):14330–44. doi:10.1364/OE.18.014330.
[11] Kester RT, Bedard N, Gao LS, Tkaczyk TS. Real-time snapshot hyperspectral imaging endoscope. J Biomed Opt 2011;16(5):056005. doi:10.1117/1.3574756.
[12] Hagen NA, Kudenov MW. Review of snapshot spectral imaging technologies. Opt Eng 2013;52(9):090901. doi:10.1117/1.OE.52.9.090901.
[13] Aasen H, Burkart A, Bolten A, Bareth G. Generating 3D hyperspectral information with lightweight UAV snapshot cameras for vegetation monitoring: from camera calibration to quality assurance. ISPRS J Photogramm Remote Sens 2015;108(5):245–59. doi:10.1016/j.isprsjprs.2015.08.002.
[14] Pittman TB, Shih YH, Strekalov DV, Sergienko AV. Optical imaging by means of two-photon quantum entanglement. Phys Rev A 1995;52(5):R3429. doi:10.1103/PhysRevA.52.R3429.

[15] Bennink RS, Bentley SJ, Boyd RW. Two-photon" coincidence imaging with a classical source. Phys Rev Lett 2002;89(11):113601. doi:10.1103/PhysRevLett.89.113601.
[16] Song SC, Sun MJ, Wu LA. Improving the signal-to-noise ratio of thermal ghost imaging based on positive-negative intensity correlation. Opt Commun 2016;366:8–12. doi:10.1016/j.optcom.2015.12.045.
[17] Radwell N, Mitchell KJ, Gibson GM, Edgar MP, Bowman R, Padgett MJ. Single-pixel infrared and visible microscope. Optica 2014;1(5):285–9. doi:10.1364/OPTICA.1.000285.
[18] Sun MJ, Edgar MP, Gibson GM, Sun B, Radwell N, Lamb R, Padgett MJ. Single-pixel three-dimensional imaging with time-based depth resolution. Nat Commun 2016;7:12010. doi:10.1038/ncomms12010.
[19] Zhang Z, Liu S, Peng J, Yao M, Zheng G, Zhong J. Simultaneous spatial, spectral, and 3D compressive imaging via efficient Fourier single-pixel measurements. Optica 2018;5(3):315–19. doi:10.1364/OPTICA.5.000315.
[20] Sun MJ, Zhang JM. Single-pixel imaging and its application in three-dimensional reconstruction: a brief review. Sensors 2019;19(3):732. doi:10.3390/s19030732.
[21] Phillips DB, Sun MJ, Taylor JM, Edgar MP, Barnett SM, Gibson GM, Padgett MJ. Adaptive foveated single-pixel imaging with dynamic supersampling. Sci Adv 2017;3(4):e1601782. doi:10.1126/sciadv.1601782.
[22] Bromberg Y, Katz O, Silberberg S. Ghost imaging with a single detector. Phys Rev A 2009;79(5):053840. doi:10.1103/physreva.79.053840.
[23] Xu ZH, Chen W, Penuelas J, Padgett M, Sun MJ. 1000 Fps computational ghost imaging using LED-based structured illumination. Opt Express 2018;26(3):2427–34. doi:10.1364/OE.26.002427.
[24] Shapiro JH. Computational ghost imaging. Phys Rev A 2008;78:061802. doi:10.1364/IQEC.2009.IThK7.
[25] Wang YW, Suo JL, Fan JT, Dai QH. Hyperspectral computational ghost imaging via temporal multiplexing. IEEE Photonics Technol Lett 2016;28(3):229–88. doi:10.1109/lpt.2015.2494878.
[26] Bian L, Suo J, Situ G, Li Z, Fan J, Chen F, Dai Q. Multispectral imaging using a single bucket detector. Sci Rep 2016;6:24752. doi:10.1038/srep24752.
[27] Liu XF, Yu WK, Yao XR, Dai B, Li LZ. Measurement dimensions compressed spectral imaging with a single point detector. Opt Commun 2016;365:173–9. doi:10.1016/j.optcom.2015.12.020.
[28] Liu Z, Tan S, Wu J, Li E, Shen X, Han S. Spectral camera based on ghost imaging via sparsity constraints. Sci Rep 2016;6(1):25718. doi:10.1038/srep25718.
[29] Deng C, Suo JL, Wang YW, Zhang ZL, Dai QH. Single-shot thermal ghost imaging using wavelength-division multiplexing. Appl Phys Lett 2018;112(5):051107. doi:10.1063/1.5001750.
[30] Duarte MF, Davenport MA, Takhar D, Laska JN, Sun T, Kelly KF. Single-pixel imaging via compressive sampling. IEEE Signal Process Mag 2008;25(2):83–91. doi:10.1364/oe.24.010476.
[31] Sun MJ, Edgar MP, Phillips DB, Gibson GM, Padgett MJ. Improving the signal-to-noise ratio of single-pixel imaging using digital microscanning. Opt Express 2016;24(10):10476–85. doi:10.1364/oe.24.010476.
[32] Ferri F, Magatti D, Lugiato LA, Gatti A. Differential ghost imaging. Phys Rev Lett 2010;104(25):253603. doi:10.1103/physrevlett.104.253603.
[33] Lochocki B, Gambín A, Manzanera S, Irles E, Artal P. Single pixel camera ophthalmoscope. Optica 2016;3(10):1056–9. doi:10.1364/optica.3.001056.
[34] Sun MJ, Meng LT, Edgar MP, Padgett MJ, Radwell N. A Russian Dolls ordering of the Hadamard basis for compressive single-pixel imaging. Sci Rep 2017;7(1):3464. doi:10.1038/s41598-017-03725-6.
[35] Rice JP, Neira JE, Kehoe M, Swanson R. DMD diffraction measurements to support design of projectors for test and evaluation of multispectral and hyperspectral imaging sensors. Proc SPIE 2009;7210. doi:10.1117/12.808990.
[36] Chen X, Yan BB, Song FJ, Wang YQ, Alameh K. Diffraction of digital micromirror device gratings and its effect on properties of tunable fiber lasers. Appl Opt 2012;51(30):7214–20. doi:10.1364/AO.51.007214.
[37] Son JY, Lee BR, Chernyshov OO, Moon KA, Lee H. Holographic display based on a spatial DMD array. Opt Lett 2013;38(16):3173–6. doi:10.1364/ol.38.003173.
[38] Wang D, Zhou EH, Brake J, Ruan H, Jang M, Yang C. Focusing through dynamic tissue with millisecond digital optical phase conjugation. Optica 2015;2(8):728–35. doi:10.1364/optica.2.000728.
[39] López-Alonso JM. Characterization of a digital-micromirror device-based infrared scene projector. Opt Eng 2005;44(8):086402. doi:10.1117/1.2013249.
[40] Duncan WM, Lee BL, Rancuret P, Sawyers BD, Endsley L, Powell D. DLP switched blaze grating: the heart of optical signal processing. Proc SPIE 2003;4983. doi:10.1117/12.480906.
[41] Petruck P, Riesenberg R, Kowarschik R. Partially coherent light-emitting diode illumination for video-rate in-line holographic microscopy. Appl Opt 2012;51(13):2333–40. doi:10.1364/ao.51.002333.
[42] Sloane NJ, Harwit M. Masks for Hadamard transform optics, and weighing designs. Appl Opt 1976;15(1):107–14. doi:10.1364/ao.15.000107.
[43] Wang Q, Allred DD, Knight LV. Deconvolution of the Raman spectrum of amorphous carbon. J Raman Spectrosc 1995;26(12):1039–43. doi:10.1002/jrs.1250261204.
[44] Courbin F, Magain P, Kirkove M, Sohy S. A method for spatial deconvolution of spectra. Astrophys J 2000;52(4):1136–44. doi:10.1086/308291.
[45] Keshava N. A survey of spectral unmixing algorithms. Linc Lab J 2003;14(1):55–78.
[46] Wei Q, Bioucas-Dias J, Dobigeon N, Tourneret JV. Hyperspectral and multispectral image fusion based on a sparse representation. IEEE Trans Geosci Remote Sens 2015;53(7):3658–68. doi:10.1109/TGRS.2014.2381272.
[47] Ghassemian H. A review of remote sensing image fusion methods. Inf Fusion 2016;32:75–89. doi:10.1016/j.inffus.2016.03.003.
[48] Pan ZW, Shen HL, Li CG, Chen SJ, John HX. Fast multispectral imaging by spatial pixel-binning and spectral unmixing. IEEE Trans Image Process 2016;25(8):3612–25. doi:10.1109/TIP.2016.2576401.
[49] Bruno TJ, Svoronos PDN. CRC handbook of fundamental spectroscopic correlation charts. CRC Press; 2005. doi:101201/9780849332500.
[50] Lu G, Fei B. Medical hyperspectral imaging a review. J Biomed Opt 2014;19(1):010901. doi:10.1117/1.JBO.19.1.010901.
[51] David L. Compressed sensing. IEEE Trans Inf Theory 2006;52(4):1289–306. doi:10.1109/TIT.2006.871582.
[52] Li LJ, Chen W, Zhao XY, Sun MJ. Fast optical phased array calibration technique for random phase modulation LiDAR. IEEE Photonics J 2019;11(1):6900410. doi:10.1109/JPHOT.2018.2889313.